

Cell-vertex WENO schemes with shock-capturing quadrature for high-order finite element discretizations of hyperbolic problems

Joshua Vedral^{a,*}, Dmitri Kuzmin^a

^a*Institute of Applied Mathematics (LS III), TU Dortmund University
Vogelpothsweg 87, D-44227 Dortmund, Germany*

Abstract

We propose a new kind of localized shock capturing for continuous (CG) and discontinuous Galerkin (DG) discretizations of hyperbolic conservation laws. The underlying framework of dissipation-based weighted essentially nonoscillatory (WENO) stabilization for high-order CG and DG approximations was introduced in our previous work. In this general framework, Hermite WENO (HWENO) reconstructions are used to calculate local smoothness sensors that determine the appropriate amount of artificial viscosity for each cell. In the original version, candidate polynomials for WENO averaging are constructed using the derivative data from von Neumann neighbors. We upgrade this standard ‘cell-cell’ reconstruction procedure by using WENO polynomials associated with mesh vertices as candidate polynomials for cell-based WENO averaging. The Hermite data of individual cells is sent to vertices of those cells, after which vertex-averaged HWENO data is sent back to cells containing the vertices. The new ‘cell-vertex’ averaging procedure includes the data of vertex neighbors without explicitly adding them to the reconstruction stencils. It mitigates mesh imprinting and can also be used in classical HWENO limiters for DG methods. The second main novelty of the proposed approach is a quadrature-driven distribution of artificial viscosity within high-order finite elements. Replacing the linear quadrature weights by their nonlinear WENO-type counterparts, we concentrate shock-capturing

*Corresponding author

Email addresses: joshua.vedral@math.tu-dortmund.de (Joshua Vedral), kuzmin@math.uni-dortmund.de (Dmitri Kuzmin)

dissipation near discontinuities while minimizing it in smooth portions of troubled cells. This redistribution of WENO stabilization preserves the total dissipation rate within each cell and improves local shock resolution without relying on subcell decomposition techniques. Numerical experiments in one and two dimensions demonstrate substantial improvements in accuracy and robustness for high-order elements, providing a compelling alternative to standard cell-cell reconstructions and subcell shock-capturing schemes.

Keywords: hyperbolic conservation laws, continuous and discontinuous Galerkin methods, cell-vertex WENO reconstruction, smoothness sensor, shock capturing, quadrature-driven dissipation

1. Introduction

Extensive research efforts have been invested over the years in the development of high-order non-oscillatory schemes for hyperbolic problems. The essentially non-oscillatory (ENO) polynomial selection principle, introduced by Harten and Osher [26], laid the foundation for stable high-order reconstructions. Shu and Osher [68, 69] further popularized ENO schemes by combining them with high-order Runge-Kutta time stepping and formulating reconstructions directly at the flux level. Building on this framework, Liu et al. [50] introduced the weighted ENO (WENO) methodology, which Jiang and Shu [34] later equipped with classical smoothness indicators and nonlinear weights, establishing the basis for most subsequent developments.

A significant line of research concerns the integration of WENO ideas into discontinuous Galerkin (DG) schemes. Qiu and Shu [64] were the first to employ WENO reconstructions as limiters for Runge-Kutta DG (RKDG) schemes, leading to a broad family of DG-WENO methods. In DG approximations, derivative information from neighboring elements is naturally available and can complement element averages in the construction of candidate polynomials. Hermite WENO (HWENO) limiters [62, 63] exploit this feature, with extensions to unstructured meshes by Zhu and Qiu [83, 86]. Luo et al. [52] demonstrated that incorporating first-order derivatives in the construction of candidate polynomials yields a simple and efficient WENO reconstruction on multidimensional unstructured grids. Zhu et al. [87] later proposed a least-squares variant of the simple WENO limiter [82].

Parallel efforts have targeted the WENO reconstruction itself. Henrick et al. [28] showed that the Jiang-Shu formulation may degrade from fifth- to

third-order accuracy at critical points and proposed a simple modification of the nonlinear weights using mapping functions to restore fifth-order accuracy. Borges et al. [11] developed higher-order global smoothness indicators via linear combination of classical ones yielding new non-oscillatory weights.

Recent developments emphasize flexibility and adaptivity of WENO schemes. Central WENO (CWENO) schemes [47, 48, 61] split the reconstruction stencil into a centered and a WENO component. WENO schemes with adaptive order (WENO-AO) [7, 8] hybridize between high-order polynomials on a centered stencil and CWENO reconstructions. Unequal-sized WENO (US-WENO) schemes [84, 85] employ artificial linear weights to avoid negative weights on unstructured grids without losing accuracy. Targeted ENO (TENO) schemes [18, 19] reduce numerical dissipation by using an ENO-like stencil selection that discards candidates crossed by discontinuities. We refer the interested reader to [56] for a comparison between classical finite volume WENO and TENO schemes for the Euler equations with gravity.

Beyond modifications of WENO reconstructions, many high-order shock-capturing methods combine a linear high-order discretization with a nonlinear WENO-type correction. Early examples include the compact upwind-ENO scheme of Adams and Shariff [2] and its WENO counterpart by Pirozzoli [60]. Hybrid centered-WENO approaches were later proposed in [29, 49, 77], and central-upwind schemes with WENO shock-capturing for systems of conservation laws were developed in [30]. In fact, the underlying idea of blending linear high-order stabilization with a nonlinear shock-capturing operator predates WENO and can be traced back to the work of Hughes et al. [31, 32], Johnson et al. [36] and Codina [14]. This general stabilization philosophy has since been expanded through nonlinear diffusion and artificial viscosity frameworks, including local projection stabilization with crosswind diffusion [9], monotonicity-preserving and graph-Laplacian stabilization methods [5, 6], and residual-based artificial viscosity methods [57].

Existing HWENO/RKDG approaches associate candidate polynomials almost exclusively with von Neumann (edge/face) neighbors. As a promising alternative, we introduce an averaging procedure in which one candidate polynomial represents the finite element approximation inside a cell, while the remaining ones represent HWENO polynomial reconstructions associated with vertices of the cell. The cell-vertex blending strategy minimizes mesh imprinting effects by incorporating vertex-neighbor information into the final cell averages. The new approach can be used both in the context of RKDG schemes equipped with HWENO limiters and in the framework of dissipation-

based WENO stabilization via nonlinear shock-capturing viscosity. The latter approach was introduced in [45] in the continuous Galerkin (CG) setting and extended to DG schemes in [74]. As a further improvement, we propose a novel quadrature-based redistribution of artificial dissipation within each cell. The weights of a standard quadrature rule are adjusted similarly to the linear weights of a WENO reconstruction, and artificial viscosity is redistributed accordingly. This enhancement of our dissipation-based WENO finite element schemes has the same effect as a localization of nonlinear stabilization to subcells [20, 27, 54, 66, 76], but is simpler and more general.

We continue in Section 2 with a review of the dissipation-based WENO stabilization methodology. The new cell-vertex reconstruction procedure and the proposed quadrature-driven localization of shock-capturing viscosity are introduced in Sections 3 and 4, respectively. In Section 5, we provide further implementation details and run numerical experiments in one and two space dimensions. The main findings are summarized in Section 6.

2. Stabilized finite element formulation

Let $u(\mathbf{x}, t)$ be a conserved quantity or a vector of conserved variables depending on the space location \mathbf{x} and time instant $t \geq 0$. For simplicity, we impose periodic boundary conditions on the boundary Γ of a spatial domain $\Omega \subset \mathbb{R}^d$, $d \in \{1, 2, 3\}$. We consider the initial value problem

$$\frac{\partial u}{\partial t} + \nabla \cdot \mathbf{f}(u) = 0 \quad \text{in } \Omega \times (0, T], \quad (1a)$$

$$u(\cdot, 0) = u_0 \quad \text{in } \Omega, \quad (1b)$$

where $\mathbf{f}(u)$ is the flux function, $T > 0$ is the final time, and u_0 is the initial datum.

2.1. Galerkin scheme

We discretize (1) in space using a CG or DG method on a conforming, possibly unstructured, affine mesh \mathcal{T}_h that consists of d -dimensional simplices or boxes K_e , $e = 1, \dots, E_h$ such that $\bar{\Omega} = \bigcup_{e=1}^{E_h} K_e$. We denote the mesh size by $h = \max_{K_e \in \mathcal{T}_h} h_e$, where $h_e = \text{diam}(K_e)$. The corresponding finite element spaces for DG and CG discretizations are defined as

$$\begin{aligned} V_{h,p}^d(\mathcal{T}_h) &:= \{v_h \in L^2(\Omega) : v_h|_{K_e} \in V_{h,p}(K_e) \forall K_e \in \mathcal{T}_h\}, \\ V_{h,p}^c(\mathcal{T}_h) &:= V_{h,p}^d(\mathcal{T}_h) \cap C^0(\bar{\Omega}), \end{aligned}$$

respectively. Here, $V_{h,p}(K_e) \in \{\mathbb{P}_p(K_e), \mathbb{Q}_p(K_e)\}$ denotes the local polynomial space of (total) degree up to $p \in \mathbb{N}$. For better readability, we omit the index p , as well as the superscripts d or c , in what follows. The simplified notation V_h will refer to either $V_{h,p}^d$ or $V_{h,p}^c$, depending on the type of the Galerkin discretization. We then seek an approximate solution of the form

$$u_h(\mathbf{x}, t) = \sum_{j=1}^{N_h} u_j(t) \varphi_j(\mathbf{x}), \quad (2)$$

where $(\varphi_j)_{j=1}^{N_h}$ is any nodal basis for V_h with polynomial degree p . The associated nodal points are denoted by $\mathbf{x}_1, \dots, \mathbf{x}_{N_h}$.

The standard Galerkin discretization of (1) yields the semi-discrete problem

$$\sum_{e=1}^{E_h} \int_{K_e} v_h \left(\frac{\partial u_h}{\partial t} + \nabla \cdot \mathbf{f}(u_h) \right) d\mathbf{x} = 0 \quad \forall v_h \in V_h. \quad (3)$$

Applying integration by parts, we rewrite (3) in the generic form

$$\frac{d}{dt}(u_h, v_h) + a(u_h, v_h) = 0 \quad \forall v_h \in V_h, \quad (4)$$

where

$$(u_h, v_h) = \sum_{e=1}^{E_h} \int_{K_e} v_h u_h d\mathbf{x} \quad (5)$$

and

$$a(u_h, v_h) = - \sum_{e=1}^{E_h} \int_{K_e} \nabla v_h \cdot \mathbf{f}(u_h) d\mathbf{x} + \sum_{e=1}^{E_h} \int_{\partial K_e} v_h \mathbf{f}(u_h) \cdot \mathbf{n} ds. \quad (6)$$

For CG methods, the second term in (6) vanishes due to continuity across element interfaces. For DG methods, the solution may be discontinuous at element boundaries, and the flux $\mathbf{f}(u_h) \cdot \mathbf{n}$ must be replaced by a Riemann solver. In this work, we use the local Lax-Friedrichs flux for scalar problems and the Harten-Lax-van Leer (HLL) flux for hyperbolic systems. Estimates of the maximum wave speed for the Euler equations can be found in [22].

2.2. Dissipative nonlinear stabilization

To ensure stability and achieve optimal convergence rates, we equip the standard Galerkin scheme (4) with the stabilization operator of the dissipation-based WENO framework [45, 74]. The stabilized formulation reads

$$\frac{d}{dt}(u_h, v_h) + a(u_h, v_h) + s_h(u_h, v_h) = 0 \quad \forall v_h \in V_h, \quad (7)$$

where the operator s_h is assembled from local element contributions as follows:

$$s_h(u_h, v_h) = \sum_{e=1}^{E_h} s_h^e(u_h, v_h). \quad (8)$$

We emphasize that this construction leaves the numerical fluxes unchanged.

The stabilization must (i) suppress spurious oscillations near discontinuities and (ii) preserve optimal accuracy in smooth regions. In the classical JST scheme [33], this is achieved by blending high- and low-order stabilization terms. The finite element version proposed in [45] uses

$$s_h^e(u_h, v_h) = \gamma_e s_h^{e,H}(u_h, v_h) + (1 - \gamma_e) s_h^{e,L}(u_h, v_h). \quad (9)$$

Here, the parameter $\gamma_e \in [0, 1]$ serves as an elementwise smoothness indicator.

Following [45, 74], we define the low-order operator as

$$s_h^{e,L}(u_h, v_h) = \nu_e \int_{K_e} \nabla v_h \cdot \nabla u_h \, d\mathbf{x}, \quad (10)$$

where ν_e is the viscosity parameter given by $\nu_e = \frac{\lambda_e h_e}{2p}$ and $\lambda_e = \|\mathbf{f}(u_h)\|_{L^\infty(K_e)}$ denotes the local maximum wave speed.

The construction of the high-order stabilization operator is somewhat more delicate. Adding an antidiffusive correction to the low-order stabilization operator (10), we obtain its high-order counterpart

$$s_h^{e,H}(u_h, v_h) = \nu_e \int_{K_e} \nabla v_h \cdot (\nabla u_h - P_h \nabla u_h) \, d\mathbf{x}, \quad (11)$$

where $P_h : L^2(\Omega) \rightarrow V_h$ is a projection operator. As shown in [75], the choice of P_h is critical for achieving optimal convergence rates.

For CG discretizations, we choose P_h to be the (componentwise) Scott-Zhang variant [67] of the Clément quasi-interpolation operator [13]. For DG methods, we use the (componentwise) L^2 orthogonal projection. In this case, $P_h \nabla u_h = \nabla u_h$ on each element, and hence $s_h^{e,H} = 0$. No high-order stabilization is required for DG methods equipped with stable numerical fluxes. For CG methods, however, some form of high-order stabilization is essential to obtain optimal convergence rates; see, e.g., [65].

Remark 1 The operator (11) is closely related to several existing stabilization techniques. In particular, it can be viewed as a component of a two-level

variational multiscale (VMS) method [35, 43, 51] and as a local fluctuation operator acting on the solution gradient, similar to those used in local projection stabilization (LPS) methods [12, 10, 37, 38]. It is also closely related to the orthogonal subscale VMS approach of Codina and Blasco [15, 16]. \square

Remark 2 For CG discretizations, the blended operator (9) can be written in the simplified form [42]

$$s_h^e(u_h, v_h) = \nu_e \int_{K_e} \nabla v_h \cdot (\nabla u_h - \gamma_e P_h \nabla u_h) \, d\mathbf{x}. \quad (12)$$

\square

The blending factor γ_e controls the interplay between the high- and low-order stabilization terms. When $\gamma_e = 0$, the nonlinear form s_h^e in (9) reduces to a low-order local Lax-Friedrichs-type diffusion. In contrast, when $\gamma_e = 1$, it recovers the high-order operator (11). For linear finite elements and the lumped-mass L^2 projection operator P_h , the bilinear form $s_h^{e,H}(u_h, v_h)$ is symmetric and positive semi-definite [58]. The consistent-mass L^2 projection provides these properties for any polynomial degree $p \geq 1$.

The smoothness sensor proposed in [45] is given by

$$\gamma_e = 1 - \min \left(1, \frac{\|u_h^e - u_h^{e,*}\|_e}{\|u_h^e\|_e} \right)^q. \quad (13)$$

We adopt this definition of γ_e , which quantifies deviations of $u_h^e := u_h|_{K_e}$ from a WENO reconstruction $u_h^{e,*}$. The exponent q controls the sensitivity of $\gamma_e \in [0, 1]$ to the relative discrepancy in the partial derivatives. The deviations are measured using the scaled Sobolev semi-norm [17, 34]

$$\|v\|_e = \left(\sum_{1 \leq |\mathbf{k}| \leq p} h_e^{2|\mathbf{k}| - d} \int_{K_e} |D^{\mathbf{k}} v|^2 \, d\mathbf{x} \right)^{1/2} \quad \forall v \in H^p(K_e), \quad (14)$$

where $\mathbf{k} = (k_1, \dots, k_d)$ denotes the multiindex of the partial derivative $D^{\mathbf{k}} v$.

By replacing the test function v_h with the basis function φ_i in the stabilized formulation (7), we obtain the semi-discrete system

$$\frac{d}{dt}(u_h, \varphi_i) + a(u_h, \varphi_i) + s_h(u_h, \varphi_i) = 0, \quad i = 1, \dots, N_h. \quad (15)$$

The numerical solution can then be advanced in time using, e.g., a strong stability preserving (SSP) Runge-Kutta method [21].

Remark 3 An element-based monolithic convex limiting (MCL) scheme for the CG version of (15) was recently developed in [42] to ensure positivity preservation. The DG version can be limited in the same way. \square

3. Cell-vertex WENO reconstruction

In principle, any standard WENO scheme from the literature can be used to reconstruct the polynomial $u_h^{e,*}$ for smoothness estimation using the shock detector (13). In our previous work [45, 74, 75], we adopted the Hermite WENO (HWENO) framework of Qiu and Shu [62] and introduced several modifications. Unlike HWENO formulations that use only cell averages and first-order derivatives [52, 62], our approach incorporates all partial derivatives up to order p , resulting in inherently compact stencils.

The procedure proposed in this section is based on the same design principles, but the candidate polynomials corresponding to finite element approximations in edge/face neighbors of a cell are replaced by WENO polynomials associated with vertices of that cell. These auxiliary polynomials are constructed using the data from cells containing the vertex. The new reconstruction procedure can be used to construct $u_h^{e,*}$ for (13) or for an HWENO limiter that overwrites the DG approximation u_h^e by $u_h^{e,*}$.

3.1. Cell-cell WENO reconstruction

One of the key challenges in designing accurate and robust WENO schemes is the choice of reconstruction stencils. In finite volume (FV) methods, high-order polynomials are fitted to the cell averages of approximate solutions in selected neighbor cells. As noted in [52, 73], the number of cells required to construct a polynomial of degree p_r in d space dimensions is

$$N_c^\Delta = \frac{(p_r + 1)(p_r + 2) \cdots (p_r + d)}{d!}, \quad N_c^\square = (p_r + 1)^d \quad (16)$$

for simplicial and tensor-product cells, respectively. Choosing appropriate stencils becomes increasingly difficult for high-order polynomials and in higher dimensions. The task becomes even more challenging on unstructured grids, which impose additional constraints on the selection of stencil cells. A detailed study of central stencil algorithms in the FV setting can be found in [73].

In the DG framework, standard WENO reconstructions from element averages of DG polynomials require FV-type stencils, which leaves the problem of identifying suitable cells unresolved. A key advantage of DG (and CG)

methods is that derivative information is readily available and can be exploited to reduce the stencil size. This idea leads to the class of Hermite WENO (HWENO) schemes, as discussed in [52, 62, 63, 83].

The l th candidate polynomial $u_{h,l}^e$ of an HWENO reconstruction for a target cell K_e uses the data of a stencil cell $K_{e'}$. The conditions

$$\frac{1}{|K_e|} \int_{K_e} u_{h,l}^e \, d\mathbf{x} = \frac{1}{|K_e|} \int_{K_e} u_h^e \, d\mathbf{x}, \quad D^{\mathbf{k}} u_{h,l}^e = D^{\mathbf{k}} u_h^{e'}, \quad 1 \leq |\mathbf{k}| \leq p_r \quad (17)$$

are satisfied by the Hermite interpolation polynomials

$$u_{h,l}^e(\mathbf{x}) = u_h^{e'}(\mathbf{x}) + \frac{1}{|K_e|} \int_{K_e} (u_h^e - u_h^{e'}) \, d\mathbf{x}, \quad \mathbf{x} \in K_e. \quad (18)$$

In this *cell-cell* version of the reconstruction procedure, each candidate polynomial is associated with a cell $K_{e'}$ that shares an edge/face $\partial K_e \cap \partial K_{e'}$ with K_e . Such cells constitute the von Neumann neighborhood of K_e .

3.2. Cell-vertex WENO scheme

The classical cell-cell construction of candidate polynomials in (17) and (18) has a key limitation: it only uses information from von Neumann neighbors and ignores vertex neighbors. The reconstruction stencils are directionally biased, because information propagates only across faces. This can be particularly problematic for oblique shocks or features not aligned with the grid. As a result, smooth regions may be misidentified, and the overall accuracy may deteriorate. A straightforward fix would be to directly include all vertex neighbors in the reconstruction stencil, which, however, increases the computational cost.

To address the above issues, we propose a vertex-based WENO reconstruction procedure, referred to as a *cell-vertex* WENO scheme. This approach incorporates information from vertex neighbors while keeping the number of candidate polynomials similar to that for traditional cell-cell approaches. The reconstruction on each element K_e is carried out in two stages. First, vertex-based candidate polynomials are constructed using WENO averaging of cell data. Second, the WENO reconstruction $u_h^{e,*}$ is defined by blending u_h^e with vertex candidates. The corresponding weights are calculated following the standard Jiang-Shu methodology. In the remainder of this section, we describe the details of our cell-vertex reconstruction procedure.

Let K_e be a mesh cell with vertices $\mathbf{x}_j \in \mathcal{V}(K_e)$, where $\mathcal{V}(K_e)$ denotes the set of all vertices of K_e , and let $v_e := |\mathcal{V}(K_e)|$ be the number of cell vertices.

For each vertex \mathbf{x}_i , we define its vertex patch $\mathcal{E}(\mathbf{x}_i) := \{K_{e'} : \mathbf{x}_i \in K_{e'}\}$ and store the indices of elements that share \mathbf{x}_i in $\mathcal{C}(\mathbf{x}_i) := \{e' : K_{e'} \in \mathcal{E}(\mathbf{x}_i)\}$.

In our cell-vertex scheme, we combine the cell candidate polynomial

$$u_{h,0}^e := u_h^e \quad (19)$$

with v_e candidate polynomials $u_{h,l}^e = u_{h,i}^*$ that are associated with the vertices $\mathbf{x}_l^e = \mathbf{x}_i$, $i \in \{1, \dots, N_h\}$ of K_e . The same vertex-based WENO reconstruction $u_{h,i}^*$ serves as a candidate polynomial for all K_e , $e \in \mathcal{C}(\mathbf{x}_i)$. The vertex candidates $u_{h,l}^e$ of a cell K_e are numbered using the local index $l \in \{1, \dots, v_e\}$.

To construct the vertex-based polynomials $u_{h,i}^*$ in a loop over $i = 1, \dots, N_h$, we exploit the fact that the restriction of the finite element solution to each element $K_{e'} \in \mathcal{E}(\mathbf{x}_i)$ coincides with the Taylor expansion [40, 53]

$$u_h^{e'}(\mathbf{x}) = \sum_{0 \leq |\mathbf{k}| \leq p} \frac{\partial^{\mathbf{k}} u_h^{e'}(\mathbf{x}_i)}{\mathbf{k}!} (\mathbf{x} - \mathbf{x}_i)^{\mathbf{k}}. \quad (20)$$

The vertex-based candidate polynomial $u_{h,l}^e$ for $\mathbf{x}_l^e = \mathbf{x}_i$ is then constructed by taking a weighted sum of these expansions over the vertex patch:

$$u_{h,i}^*(\mathbf{x}) = \sum_{e' \in \mathcal{C}(\mathbf{x}_i)} \omega_{e'}^i u_h^{e'}(\mathbf{x}) = \sum_{0 \leq |\mathbf{k}| \leq p} \frac{(\mathbf{x} - \mathbf{x}_i)^{\mathbf{k}}}{\mathbf{k}!} \sum_{e' \in \mathcal{C}(\mathbf{x}_i)} \omega_{e'}^i \partial^{\mathbf{k}} u_h^{e'}(\mathbf{x}_i). \quad (21)$$

Thus, $u_{h,i}^*$ is a convex combination of Taylor polynomials representing the finite element solution in cells around \mathbf{x}_i . The stencils used in the cell-based and vertex-based polynomial reconstructions are illustrated in Fig. 1.

The candidate polynomials defined in (21) do not necessarily preserve the cell average of the finite element solution on K_e . This is not an issue, since the smoothness indicator γ_e in (13) depends only on the derivatives of the candidate polynomials. However, the cell averages can be corrected similarly to (18). The resulting candidate polynomials, which now preserve the cell average on K_e , read

$$\bar{u}_{h,i}^*(\mathbf{x}) = \sum_{e' \in \mathcal{C}(\mathbf{x}_i)} \omega_{e'}^i u_h^{e'}(\mathbf{x}) + \frac{1}{|K_e|} \int_{K_e} (u_h^e - \sum_{e' \in \mathcal{C}(\mathbf{x}_i)} \omega_{e'}^i u_h^{e'}) \, d\mathbf{x}. \quad (22)$$

The nonlinear weights for vertex-based WENO averaging in (21) are calculated using equal linear weights in the Jiang-Shu formula [34] such that

$$\omega_{e'}^i = \frac{\tilde{\omega}_{e'}^i}{\sum_{e \in \mathcal{C}(\mathbf{x}_i)} \tilde{\omega}_e^i}, \quad \tilde{\omega}_e^i = \frac{1}{(\varepsilon + \beta_e^i)^r}, \quad (23)$$

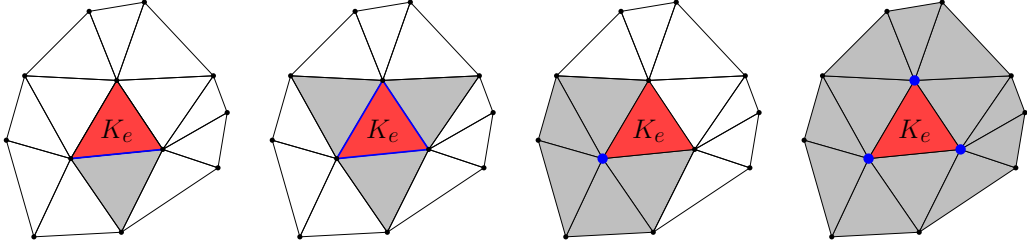


Figure 1: Candidate polynomial stencils for triangular elements. The left two figures show cell-cell stencils. The first one illustrates the cell-based stencil for a single candidate polynomial, while the second one displays the full stencil of a cell-cell reconstruction. The right two figures present the corresponding vertex-based and cell-vertex stencils. In both approaches, four candidate polynomials are used, including the finite element approximation u_h^e in the target cell K_e .

where $\varepsilon > 0$ prevents division by zero, β_e^i are pointwise smoothness indicators, and $r > 0$ is a positive integer. Following Jiang and Shu [34], we set $\varepsilon = 10^{-6}$ and $r = 2$. The smoothness indicators are given by

$$\beta_e^i = \|u_h^e\|_{\mathbf{x}_i}^q, \quad q \geq 1, \quad (24)$$

where the vertex-based semi-norm

$$\|v\|_{\mathbf{x}_i} = \left(\sum_{1 \leq |\mathbf{k}| \leq p} h_e^{2|\mathbf{k}|} |D^{\mathbf{k}} v(\mathbf{x}_i)|^2 \right)^{1/2} \quad \forall v \in H^s(K_e) \quad (25)$$

is the pointwise analogue of the element-level semi-norm in (14). By the Sobolev embedding theorem, this semi-norm is well-defined for $s > p + d/2$.

Having constructed all vertex-based candidate polynomials $u_{h,i}^*$ in the loop over $i = 1, \dots, N_h$, we enter a loop over the cell indices $e = 1, \dots, E_h$. In this loop, we calculate the final cell-vertex WENO reconstructions

$$u_h^{e,*} = \sum_{l=0}^{v_e} \omega_l^e u_{h,l}^e \in \mathbb{P}_p(K_e). \quad (26)$$

The cell candidate $u_{h,0}^e = u_h^e$ and vertex candidates $u_{h,l}^e$, $l = 1, \dots, v_e$ corresponding to $u_{h,i}^*$, $i = i(l) \in \mathcal{V}(K_e)$ are averaged using the nonlinear weights

$$\omega_l^e = \frac{\tilde{\omega}_l^e}{\sum_{j=0}^{v_e} \tilde{\omega}_j^e}, \quad \tilde{\omega}_l^e = \frac{\gamma_l^e}{(\varepsilon + \beta_l^e)^r}. \quad (27)$$

In the above definition of $\tilde{\omega}_l^e$, the smoothness indicators [17, 34]

$$\beta_l^e = \|u_{h,l}^e\|_e^q, \quad q \geq 1 \quad (28)$$

use the element-level semi-norm from (14). Following standard practice, we again set $\varepsilon = 10^{-6}$ and $r = 2$. The linear weights γ_l^e can be any positive numbers that sum to one. We assign small linear weights $\gamma_l^e = 10^{-3}$ to the vertex-based candidates $u_{h,l}^e$ for $l = 1, \dots, v_e$, while the cell candidate $u_{h,0}^e = u_h^e$ receives the dominant weight $\gamma_0^e = 1 - \sum_{l=1}^{v_e} \gamma_l^e$, ensuring that the reconstruction reduces to the finite element solution in smooth regions.

Remark 4 When it comes to evaluating the WENO reconstruction (26) at $\mathbf{x} \in K_e$, we transform the Taylor basis representation (21) of each vertex candidate $u_{h,l}^e = u_{h,i}^*$ into the finite element basis used for the representation of the cell candidate $u_{h,0}^e$. Using the same basis for all $v_e + 1$ candidates is particularly convenient for computing the smoothness sensor γ_e in (13). \square

Remark 5 The size of candidate stencils that we use in each stage of the cell-vertex approach is comparable to that of a single-stage cell-cell reconstruction. Specifically, both versions use three candidates in one dimension, four candidates for triangles, and five candidates for quadrilaterals and tetrahedra. For cubes, the vertex-based approach slightly increases the number of candidates from six to eight. On unstructured meshes, a minimum-angle condition imposes an upper bound on the number of elements that may meet at a vertex. In contrast to cell-cell reconstructions [73, 88], the cell-vertex stencils are uniquely determined by the connectivity pattern of the mesh, and the WENO averaging can be coded using standard data structures. \square

4. Shock-capturing WENO quadrature

In the dissipation-based WENO framework of Section 2, the smoothness sensor γ_e controls the amount of artificial viscosity added to the Galerkin discretization. Since γ_e is constant on each element, the corresponding dissipation is distributed uniformly on K_e . For high-order elements on coarse meshes, however, it is often desirable to localize the dissipation within an element, concentrating it near sharp gradients or discontinuities. We propose a novel WENO-inspired strategy that accomplishes this by rescaling the weights of the quadrature rule for calculating the stabilization term (9). Unlike subcell-based localization approaches [24, 44, 59, 71], our method requires no

additional subcell decompositions/computations. It simply redistributes the total dissipation added in K_e among the quadrature points.

Let $D_e = s_h^e(u_h, u_h)$ denote the elementwise dissipation rate for s_h^e defined by (9). In the DG setting, D_e can be written as

$$D_e^{\text{DG}} = (1 - \gamma_e) \nu_e \int_{K_e} |\nabla u_h|^2 \, d\mathbf{x} = \nu_e \int_{K_e} (|\nabla u_h|^2 - \gamma_e |\nabla u_h|^2) \, d\mathbf{x} \quad (29)$$

and in the CG setting as

$$D_e^{\text{CG}} = \nu_e \int_{K_e} (|\nabla u_h|^2 - \gamma_e \nabla u_h \cdot P_h \nabla u_h) \, d\mathbf{x}. \quad (30)$$

If $s_h^e(u_h, v_h)$ is calculated using a quadrature rule with weights ω_q and nodes \mathbf{x}_q , $q = 1, \dots, N_q$, both expressions take the unified form

$$D_e^{\text{orig}} = \nu_e \sum_{q=1}^{N_q} \omega_q f_q, \quad (31)$$

where $f_q = (1 - \gamma_e) |\nabla u_h(\mathbf{x}_q)|^2$ in the DG setting and $f_q = |\nabla u_h(\mathbf{x}_q)|^2 - \gamma_e \nabla u_h \cdot P_h \nabla u_h$ in the CG setting.

To localize the WENO dissipation, we introduce nonlinear scaling factors α_q and calculate $s_h^e(u_h, v_h)$ using the weights $\alpha_q \omega_q$ instead of ω_q . This adjustment of the quadrature rule has the effect of replacing D_e^{orig} with

$$D_e^{\text{scaled}} = \nu_e \sum_{q=1}^{N_q} \omega_q \alpha_q f_q. \quad (32)$$

The total dissipation must remain unchanged. This is enforced by defining

$$\alpha_q := \frac{\tilde{\alpha}_q \sum_{r=1}^{N_q} \omega_r f_r}{\sum_{r=1}^{N_q} \omega_r \tilde{\alpha}_r f_r}, \quad (33)$$

where the preliminary weights

$$\tilde{\alpha}_q := \frac{\|u_h\|_{\mathbf{x}_q}}{\|u_h\|_e} \quad (34)$$

serve as WENO-type smoothness indicators that allocate more dissipation to quadrature nodes near sharp features.

The above choice of the redistribution weights α_q preserves the dissipation rate D_e^{orig} exactly. Indeed, substituting (33) into (32) gives

$$D_e^{\text{scaled}} = \nu_e \sum_{q=1}^{N_q} \omega_q \left(\frac{\tilde{\alpha}_q \sum_{r=1}^{N_q} \omega_r f_r}{\sum_{r=1}^{N_q} \omega_r \tilde{\alpha}_r f_r} \right) f_q = \frac{\nu_e \sum_{r=1}^{N_q} \omega_r f_r}{\sum_{r=1}^{N_q} \omega_r \tilde{\alpha}_r f_r} \sum_{q=1}^{N_q} \omega_q \tilde{\alpha}_q f_q. \quad (35)$$

Using the identity $\nu_e \sum_{r=1}^{N_q} \omega_r f_r = D_e^{\text{orig}}$, we find that

$$D_e^{\text{scaled}} = \frac{D_e^{\text{orig}}}{\sum_{r=1}^{N_q} \omega_r \tilde{\alpha}_r f_r} \sum_{q=1}^{N_q} \omega_q \tilde{\alpha}_q f_q = D_e^{\text{orig}}. \quad (36)$$

Furthermore, the adjustment of the quadrature weights does not affect the zero sum property $s_h^e(u_h, 1) = 0$ that ensures discrete conservation.

The redistribution affects the solution only when a noticeable level of artificial viscosity is present. For smooth elements, where γ_e is small and the added dissipation is negligible, the scaling has little impact on the results. In practice, it is therefore worthwhile to redistribute only when $D_e^{\text{orig}} > C_{D_e^{\text{orig}}}$ or $\gamma_e < C_{\gamma_e}$, where $C_{D_e^{\text{orig}}}$ and C_{γ_e} are prescribed cutoff parameters.

Remark 6 For linear finite elements, the gradient of u_h is piecewise constant. Therefore, the preliminary weights (34) are all equal to $\tilde{\alpha}_q = 1/|K_e|$ and the WENO weights (33) are all equal to unity. Hence, no redistribution is performed in the case $p = 1$. For a finite element of degree $p > 1$, the gradient is a polynomial of degree $p - 1$. Hence, the distribution of normalized scaling factors is nonuniform, as shown in Fig. 2. The WENO formula (33) assigns larger weights α_q to quadrature points \mathbf{x}_q at which the pointwise derivative sensor $\|u_h\|_{\mathbf{x}_q}$ is large compared to the cell average $\|u_h\|_e/|K_e|$. \square

5. Numerical results

In this section, we present numerical results for standard hyperbolic test problems, including linear and nonlinear scalar equations and the Euler equations of gas dynamics. We assess the shock-capturing capabilities of our method as well as its accuracy in smooth solution regimes for both continuous and discontinuous finite element discretizations. Moreover, we verify that the proposed scheme does not produce entropy-violating solutions and highlight its advantages over existing high-order *cell-cell* WENO schemes, particularly for large polynomial degrees.

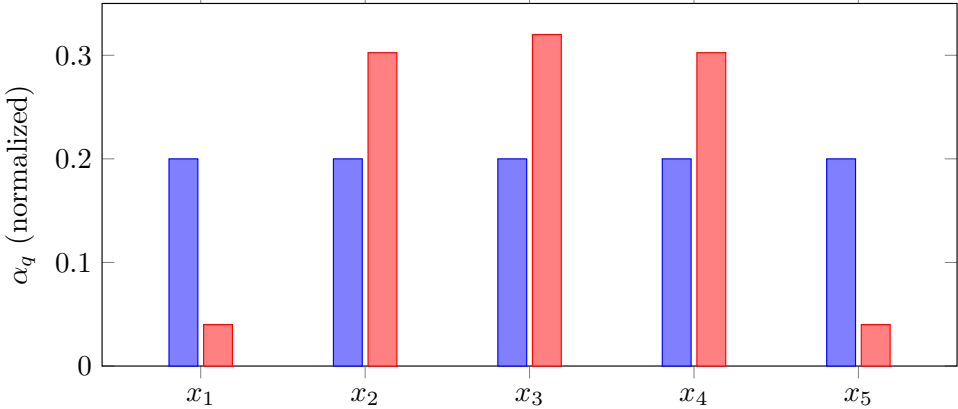


Figure 2: Normalized scaling factors $\alpha_q / \sum_{r=1}^{N_q} \alpha_r$ for a one-dimensional fifth-order finite element containing a discontinuity at its center. The uniform scaling (blue) uses $\alpha_q = 1$. The WENO scaling (red) uses the weights α_q given by (33).

For clarity, we refer to the *cell-cell* WENO schemes from [45, 75] as CC-WENO. The *cell-vertex* WENO scheme proposed in Sec. 3 is denoted by CV-WENO. We write CV-WENO-SC for the CV-WENO scheme equipped with shock-capturing WENO quadrature, as introduced in Sec. 4.

All numerical experiments are performed on uniform structured meshes. Extensions to unstructured meshes and three-dimensional problems will be reported elsewhere. The steepening parameter in (13) is set to $q = 1$. To avoid unnecessary rescaling of the weights in the WENO quadrature procedure, we only employ the shock-capturing WENO quadrature when $\gamma_e < C_{\gamma_e}$ with $C_{\gamma_e} = 0.9$. We use \mathbb{Q}_p Lagrange finite elements with polynomial degree $p \geq 1$. To enable a fair comparison across different polynomial orders, the total number of degrees of freedom N_h is kept fixed by coarsening the mesh as p increases.

Spatial discretization errors are measured using the L^1 norm and experimental orders of convergence (EOC) are computed following [46, 51]. Time integration is performed using the third-order strong stability preserving (SSP) Runge-Kutta method [21] with time steps chosen sufficiently small so that temporal errors are negligible relative to spatial discretization errors.

All computations are carried out using the C++ finite element library MFEM [3, 4, 55] and the results to two-dimensional problems are visualized using the C++ software GLVis [1].

5.1. Solid body rotation

In our first numerical experiment, we consider LeVeque's solid body rotation problem [46], which is used to assess a method's capability to capture smooth and discontinuous features of an exact solution to the linear advection equation

$$\frac{\partial u}{\partial t} + \nabla \cdot (\mathbf{v}u) = 0 \quad \text{in } \Omega = (0, 1)^2$$

with the velocity field $\mathbf{v}(x, y) = (0.5 - y, x - 0.5)^\top$. The initial and boundary conditions are taken from [41, 46]. Since the exact solution is periodic in time, it coincides with the initial condition after each full revolution $t \in \mathbb{N}$, and we stop computations at the final time $t = 1$.

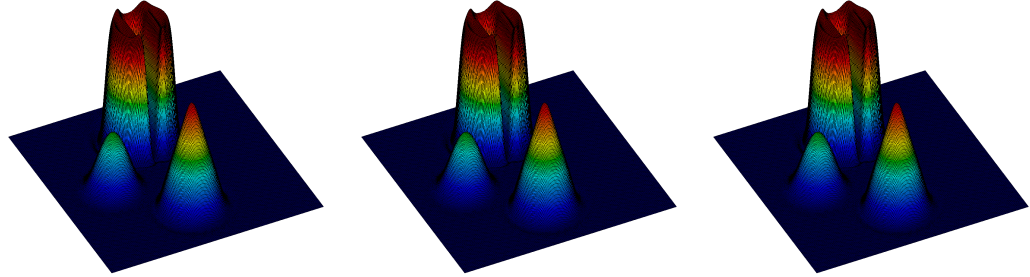
We use the mesh size h corresponding to $N_h = 257^2$ DoFs for a given polynomial degree p , and employ continuous finite elements. The results are shown in Fig. 3. For linear and quadratic polynomials, the new CV-WENO variant produces solutions comparable to classical CC-WENO schemes. For quartic Lagrange polynomials, however, the CV-WENO scheme reproduces both smooth and discontinuous solution features far more accurately, while the CC-WENO scheme exhibits a clear loss of accuracy. This behavior has previously been reported in [45] and the reason for this is twofold. First, the CC-WENO reconstruction only uses information from von Neumann neighbors and excludes vertex neighbors, resulting in a significant loss of spatial information that becomes increasingly severe for higher polynomial degrees and coarser meshes. Second, the CC-WENO scheme extrapolates high-order polynomials from neighboring elements into the target element, a procedure that becomes increasingly ill-posed as the polynomial degree increases. The CV-WENO scheme resolves both issues.

As shown in Table 1, equipping the CV-WENO scheme with shock-capturing WENO quadrature reduces the L^1 errors compared to the standard CV-WENO formulation.

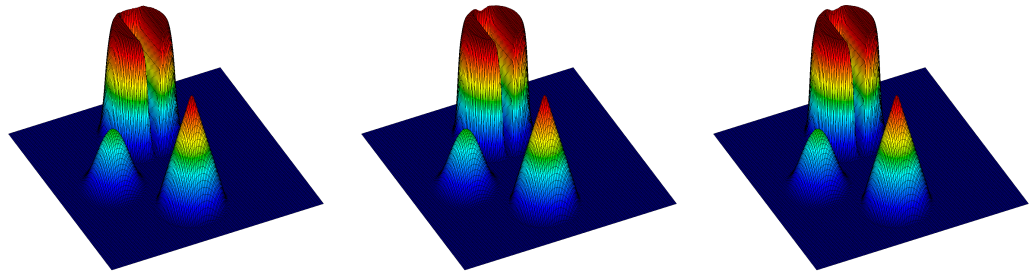
	$p = 1$	$p = 2$	$p = 4$
CC-WENO	1.60595e-02	1.57469e-02	5.43568e-02
CV-WENO	1.59866e-02	1.18561e-02	1.17923e-02
CV-WENO-SC	1.59861e-02	1.17689e-02	1.08783e-02

Table 1: Errors $\|u_h - u_{\text{ex}}\|_{L^1(\Omega)}$ to the solid body rotation problem [46] at $t = 1$ obtained using $N_h = 257^2$ and $p \in \{1, 2, 4\}$.

(a) CC-WENO, $p = 1$, $u_h \in [-0.06179, 1.08641]$ (b) CV-WENO, $p = 1$, $u_h \in [-0.06710, 1.08863]$ (c) CV-WENO-SC, $p = 1$, $u_h \in [-0.06711, 1.08865]$



(d) CC-WENO, $p = 2$, $u_h \in [-0.00439, 1.00751]$ (e) CV-WENO, $p = 2$, $u_h \in [-0.00975, 1.00819]$ (f) CV-WENO-SC, $p = 2$, $u_h \in [-0.00984, 1.00832]$



(g) CC-WENO, $p = 4$, $u_h \in [-1.7e-05, 0.85188]$ (h) CV-WENO, $p = 4$, $u_h \in [-0.00310, 1.00466]$ (i) CV-WENO-SC, $p = 4$, $u_h \in [-0.05656, 1.02060]$

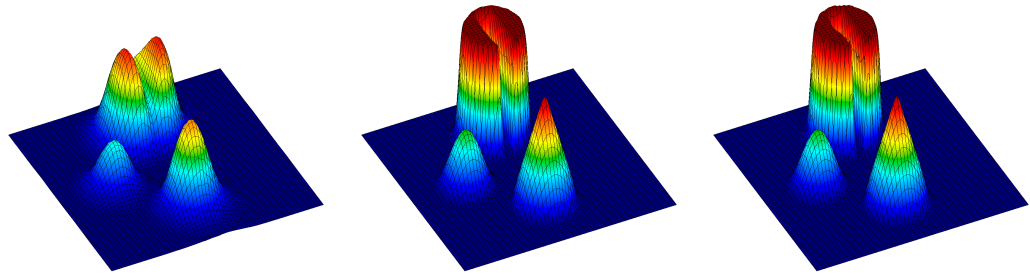


Figure 3: Numerical solutions to the solid body rotation problem [46] at $t = 1$ obtained using $N_h = 257^2$ and $p \in \{1, 2, 4\}$.

E_h	$p = 1$	EOC	$p = 2$	EOC	$p = 3$	EOC
48	1.76E-03		5.30E-05		1.43E-05	
64	7.73E-04	2.86	2.35E-05	2.83	7.27E-06	2.35
96	2.72E-04	2.58	8.21E-06	2.59	2.93E-06	2.24
128	1.45E-04	2.19	3.87E-06	2.61	1.50E-06	2.33
192	6.50E-05	1.98	1.21E-06	2.87	4.79E-07	2.82
256	3.67E-05	1.99	4.82E-07	3.20	1.76E-07	3.48
384	1.64E-05	1.99	1.21E-07	3.41	3.75E-08	3.81
512	9.23E-06	2.00	4.59E-08	3.37	1.21E-08	3.93
768	4.11E-06	2.00	1.22E-08	3.27	2.46E-09	3.93
1024	2.31E-06	2.00	4.87E-09	3.19		
1536	1.03E-06	1.99				

Table 2: $L^1(\Omega)$ error norms and convergence rates for the CC-WENO scheme applied to the 1D inviscid Burgers equation with initial condition (37) at $t = 0.1$.

5.2. One-dimensional inviscid Burgers equation

In the next experiment, we solve the one-dimensional inviscid Burgers equation

$$\frac{\partial u}{\partial t} + \frac{\partial(u^2/2)}{\partial x} = 0 \quad \text{in } \Omega = (0, 1).$$

The initial condition

$$u_0(x) = \sin(2\pi x) \tag{37}$$

remains smooth up to the critical time $t_c = \frac{1}{2\pi}$ of shock formation. We perform grid convergence studies at $t = 0.1$, for which the solution is sufficiently smooth, and report the results in Tables 2 and 3. The time step is chosen small enough to make the spatial error dominant. As before, we use continuous Lagrange finite elements. Since the shock-capturing WENO quadrature is inactive in smooth regions, the numerical errors produced by the CV-WENO and CV-WENO-SC scheme are identical and therefore reported only once. It is observed that all methods achieve optimal convergence rates. Moreover, consistent with the behavior observed for the linear solid body rotation benchmark, CV-WENO outperforms CC-WENO on coarse meshes and reaches the asymptotic regime faster.

Remark 7 Similar convergence behavior is observed for the one-dimensional linear advection equation with a smoothed step function, taken from [25, Sec. 7.1], using a constant velocity $v = 1$ (not shown here). As before, all

E_h	$p = 1$	EOC	$p = 2$	EOC	$p = 3$	EOC
48	1.83E-03		4.70E-05		4.03E-06	
64	7.59E-04	3.06	1.91E-05	3.13	1.33E-06	3.85
96	2.66E-04	2.59	5.54E-06	3.05	2.73E-07	3.91
128	1.45E-04	2.11	2.32E-06	3.03	8.84E-08	3.92
192	6.50E-05	1.98	6.81E-07	3.02	1.80E-08	3.93
256	3.67E-05	1.99	2.87E-07	3.00	5.85E-09	3.91
384	1.64E-05	1.99	8.48E-08	3.01	1.21E-09	3.89
512	9.22E-06	2.00	3.57E-08	3.01	3.96E-10	3.88
768	4.11E-06	1.99	1.06E-08	2.99	8.29E-11	3.86
1024	2.31E-06	2.00	4.46E-09	3.01		
1536	1.03E-06	1.99				

Table 3: $L^1(\Omega)$ error norms and convergence rates for the CV-WENO(-SC) scheme applied to the 1D inviscid Burgers equation with initial condition (37) at $t = 0.1$.

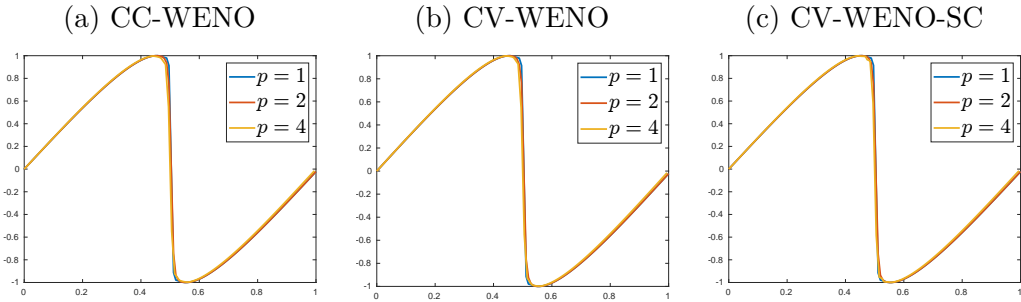


Figure 4: Numerical solutions to the 1D inviscid Burgers equation at $t = 0.2$ obtained using $N_h = 128$ and $p \in \{1, 2, 4\}$.

schemes converge at the optimal rate $p + 1$. The DG variant of the proposed methods also exhibits optimal convergence at the same rate. \square

By extending the final time to $t = 1 > t_c$, after the shock has fully developed, we assess the shock-capturing properties of the schemes. With the total number of degrees of freedom fixed at $N_h = 128$, the results in Fig. 4 show that all WENO schemes produce nonoscillatory solutions with nearly identical profiles and increasing the polynomial degree p has little effect. Due to the self-steepening nature of shock fronts, relatively diffusive schemes perform well in this benchmark. Even the uniform choice $\gamma_e = 1$ in (9), which corresponds to a low-order Lax-Friedrichs-type scheme, yields satisfactory results, as reported in [45, 74].

5.3. KPP problem

In the next experiment, we consider the KPP problem [39], a challenging nonlinear test problem for assessing entropy stability of high-order numerical schemes. We solve (1a) with the nonconvex flux function $\mathbf{f}(u) = (\sin(u), \cos(u))$ on the computational domain $\Omega = (-2, 2) \times (-2.5, 1.5)$. The initial condition

$$u_0(x, y) = \begin{cases} \frac{7\pi}{2} & \text{if } \sqrt{x^2 + y^2} \leq 1, \\ \frac{\pi}{4} & \text{otherwise,} \end{cases}$$

generates an exact entropy solution exhibiting a rotational wave structure. Standard schemes often fail to converge to the exact entropy solution without an appropriate entropy fix. For dissipation-based methods, introducing sufficient dissipation near shocks is essential to converge to the correct entropy solution. A global upper bound for the maximum wave speed, required to compute the viscosity parameter ν_e in (10), is given by $\lambda_e = 1.0$. More accurate bounds can be found in [23].

Simulations are performed on a uniform mesh with $N_h = 257^2$ DoFs using continuous Lagrange finite elements of order $p = 2$. The results, shown in Fig. 5, indicate that the CV-WENO scheme produces nonoscillatory solutions that accurately capture the spiral wave structure, with accuracy comparable to the CC-WENO variant. The results for $p = 1$ and $p = 4$ (not shown here) are similar. Although a (semi-)discrete entropy inequality cannot be formally proven for our scheme, as is the case for most WENO schemes reported in the literature, the results suggest that it is at least numerically entropy stable.

5.4. Euler equations of gas dynamics

We consider the Euler equations of gas dynamics which describe the conservation of mass, momentum and total energy. The vector of conserved variables and the corresponding flux tensor in (1a) are given by

$$U = \begin{bmatrix} \varrho \\ \varrho \mathbf{v} \\ \varrho E \end{bmatrix} \in \mathbb{R}^{d+2}, \quad \mathbf{F}(\mathbf{U}) = \begin{bmatrix} \varrho \mathbf{v} \\ \varrho \mathbf{v} \otimes \mathbf{v} + p \mathbf{I} \\ (\varrho E + p) \mathbf{v} \end{bmatrix} \in \mathbb{R}^{(d+2) \times d},$$

where ϱ , \mathbf{v} , E denote the density, velocity and specific total energy, respectively. The identity matrix is denoted by \mathbf{I} . The pressure p is calculated using the polytropic ideal gas law

$$p = \varrho e(\gamma - 1),$$

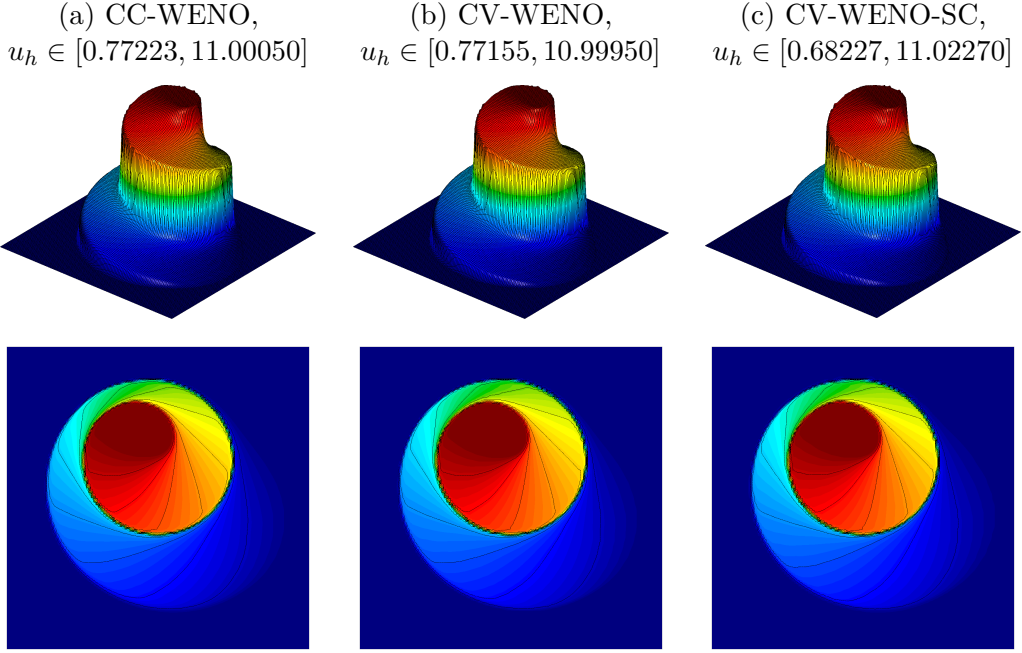


Figure 5: Numerical solutions to the KPP problem [39] at $t = 1$ obtained using $N_h = 257^2$ and $p = 2$.

where ϱe and γ denote the internal energy and the heat capacity ratio, respectively. In all numerical experiments, we set $\gamma = 1.4$.

Following the approach in [45, 74], the blending factor γ_e in (13) is computed from the density field and subsequently applied to all variables, yielding significant computational savings without compromising robustness, as reported in [60].

In what follows, we do not present results obtained with the CC-WENO scheme. Numerical solutions of the Euler equations using CC-WENO are available in [74] for the DG formulation and in the recent work [42] for the CG formulation.

5.4.1. Modified Sod shock tube

We assess the entropy stability of our scheme for hyperbolic systems using the modified Sod shock tube problem [72], a modification of the classical Sod

shock tube [70]. The initial conditions are prescribed as

$$(\rho_0, v_0, p_0)(x) = \begin{cases} (1, 0.75, 1) & \text{if } x < 0.25, \\ (0.125, 0, 0.1) & \text{otherwise,} \end{cases}$$

within the computational domain $\Omega = (0, 1)$. The left boundary at $x = 0$ acts as a supersonic inlet, while the right boundary at $x = 1$ is reflective. The initial discontinuity at $x = 0.25$ generates a rarefaction wave, a contact discontinuity, and a shock, all of which the numerical scheme should resolve accurately. High-order methods are known to produce entropy glitches near the sonic point of the rarefaction wave, highlighting the importance of robust entropy-stable methods.

We run simulations up to the final time $t = 0.2$ on uniform meshes. Although DG finite elements are commonly regarded as better suited for hyperbolic problems than CG finite elements, we investigate this assumption through our numerical tests. Both approaches are compared using roughly the same number of degrees of freedom per variable ($N_{h,1} = 257$ for CG and $N_{h,2} = 256$ for DG) to ensure a fair evaluation. We further aim to demonstrate that our scheme can handle very high-order polynomials.

The numerical results obtained with the CV-WENO and CV-WENO-SC variants, using continuous and discontinuous finite elements, are shown in Figs. 6 and 7, respectively. The results indicate that the CG formulation of the CV-WENO strategy performs comparably to its DG counterpart in terms of accuracy and shock-capturing properties. Remarkably, we obtain reasonable solutions even for polynomial degrees as high as $p = 32$ on only eight elements. The shock-capturing quadrature produces less smearing near the rarefaction wave. Moreover, for all polynomial degrees and for both CG and DG formulations, the numerical solutions remain entropy stable, eliminating the need for additional (semi-)discrete entropy fixes. These findings are consistent with the observations from the KPP problem.

5.4.2. Woodward-Colella blast wave problem

The next numerical test we consider is the Woodward-Colella blast wave problem [78], a challenging benchmark for assessing the robustness of numerical schemes due to the presence of strong discontinuities in the initial pressure

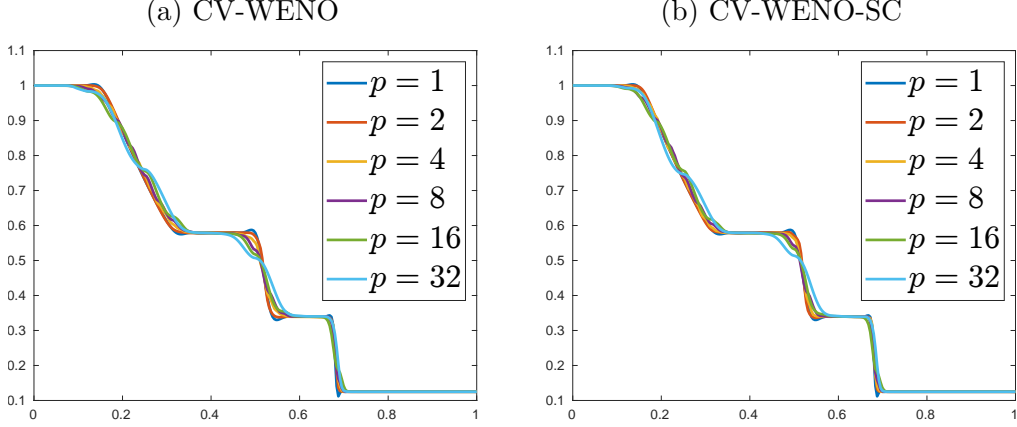


Figure 6: Modified Sod shock tube, density profiles ϱ at $t = 0.2$ obtained using continuous finite elements with $N_h = 257$ DoFs per variable.

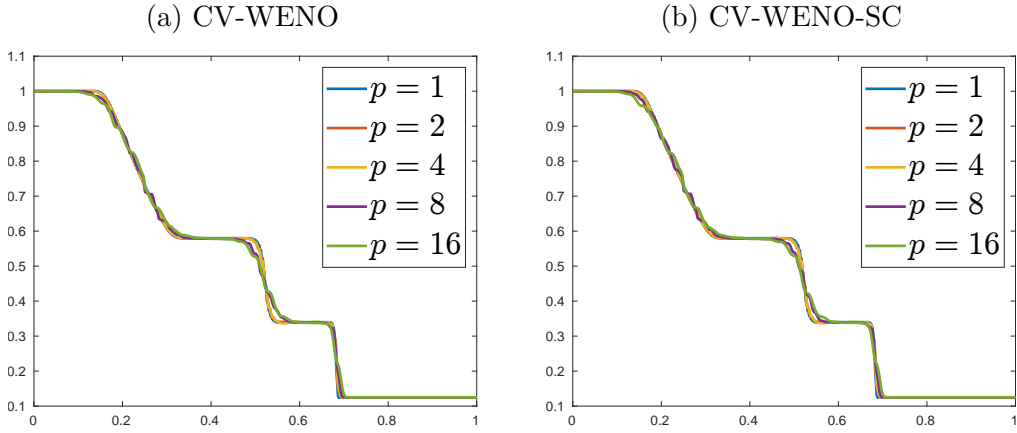


Figure 7: Modified Sod shock tube, density profiles ϱ_h at $t = 0.2$ obtained using discontinuous finite elements with $N_h = 256$ DoFs per variable.

distribution

$$p_0(x) = \begin{cases} 1000 & \text{if } 0 < x < 0.1, \\ 0.01 & \text{if } 0.1 \leq x \leq 0.9, \\ 100 & \text{if } 0.9 < x < 1. \end{cases}$$

The computational domain is $\Omega = (0, 1)$ and bounded by reflective walls. The initial density is constant throughout the domain, $\varrho \equiv 1$, and the fluid is initially at rest, i.e., $v_0 \equiv 0$. Simulations are carried out up to the final

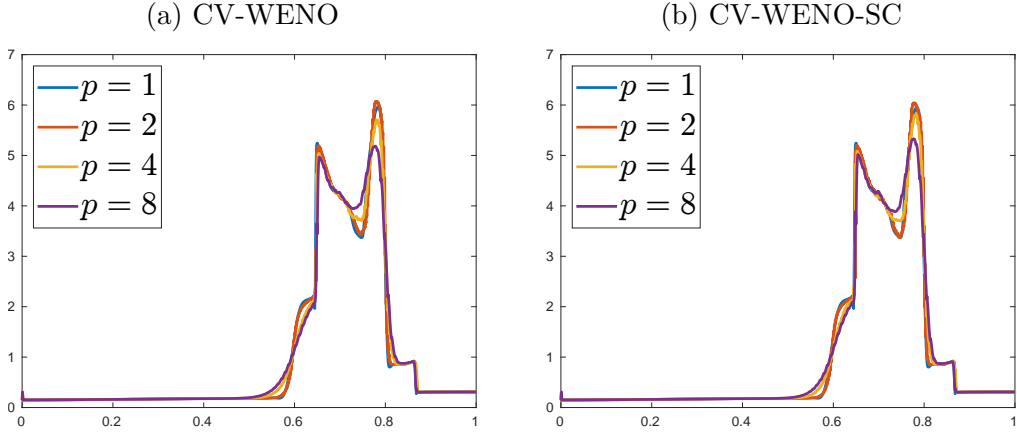


Figure 8: Woodward-Colella blast wave problem, density profiles ϱ_h at $t = 0.038$ obtained using continuous finite elements with $N_h = 1025$ DoFs per variable.

time $t = 0.038$, by which the two initial Riemann problems have evolved into a complex flow featuring multiple interactions between strong shock waves, rarefaction waves, and contact discontinuities. Consequently, no exact solution is available for this problem.

We investigate the differences between the CV-WENO and CV-WENO-SC methods in terms of solution accuracy and shock-capturing capabilities using continuous finite elements. Figure 8 shows the numerical solutions obtained for various polynomial degrees p , using $N_h = 1025$ degrees of freedom per variable. The CV-WENO scheme is sufficiently robust to maintain positivity of density and pressure, so that no additional flux and/or slope limiters are required to ensure invariant domain preservation (IDP). It accurately captures the right density peak, which is slightly better resolved with $p = 2$ than with $p = 1$, consistent with the findings in [42]. Notably, the shock-capturing WENO quadrature has little effect for $p \leq 2$, but for $p = 4$ and $p = 8$ the right density peak is captured more accurately when the shock-capturing WENO quadrature is activated.

5.4.3. Double Mach reflection

In our final numerical experiment, we consider the double Mach reflection problem introduced by Woodward and Colella [78], which represents a challenging benchmark for multidimensional shock-capturing schemes. The computational domain is $\Omega = (0, 4) \times (0, 1)$. The pre-shock and post-shock

states are given by

$$(\varrho_L, v_{x,L}, v_{y,L}, p_L) = (8.0, 8.25 \cos(30^\circ), -8.25 \sin(30^\circ), 116.5), \\ (\varrho_R, v_{x,R}, v_{y,R}, p_R) = (1.4, 0.0, 0.0, 1.0),$$

and are used to prescribe both the initial condition and the inflow boundary data. At the initial time, the post-shock state (subscript L) is imposed in the domain $\Omega_L = \{(x, y) \mid x < \frac{1}{6} + \frac{y}{\sqrt{3}}\}$, while the pre-shock state (subscript R) is prescribed in the complementary domain $\Omega_R = \Omega \setminus \Omega_L$. The reflecting wall corresponds to the boundary segment $y = 0$ for $1/6 \leq x \leq 4$. No boundary conditions are required at the outflow boundary $x = 4$. Along the remaining parts of the boundary, post-shock conditions are imposed for $x < \frac{1}{6} + \frac{1+20t}{\sqrt{3}}$, while pre-shock conditions are prescribed elsewhere. This construction ensures that the motion of the initial Mach 10 shock along the top boundary is represented exactly.

The resulting flow configuration features a Mach 10 shock in air impinging on a reflecting wall at an initial angle of 60° . A robust numerical scheme must accurately resolve the triple-point region, while simultaneously capturing strong shocks without generating spurious oscillations.

Figure 9 shows snapshots of the density field at the final time $t = 0.2$, computed using discontinuous finite elements on a mesh consisting of $E_h = 384 \cdot 96$ elements with $p = 2$. To prevent the occurrence of negative pressures during the simulation, we additionally employ the Zhang-Shu limiter [79]. While alternative parameter choices in the WENO reconstruction may lead to IDP solutions, the scheme is not guaranteed to be IDP in general. Both the CV-WENO and CV-WENO-SC variants successfully resolve the triple-point region while introducing sufficient numerical dissipation to suppress non-physical oscillations.

Remark 8 The recent work [42] proposes a continuous Galerkin extension of the Zhang-Shu limiting framework [79, 80, 81], which can be employed to render the CG formulation of the CV-WENO scheme provably IDP. Results along these lines will be reported elsewhere. \square

6. Conclusions

We presented a vertex-centered WENO approach for dissipative stabilization of high-order finite element schemes, enhanced by an adaptive WENO-based scaling of quadrature weights. In our scheme, candidate polynomials

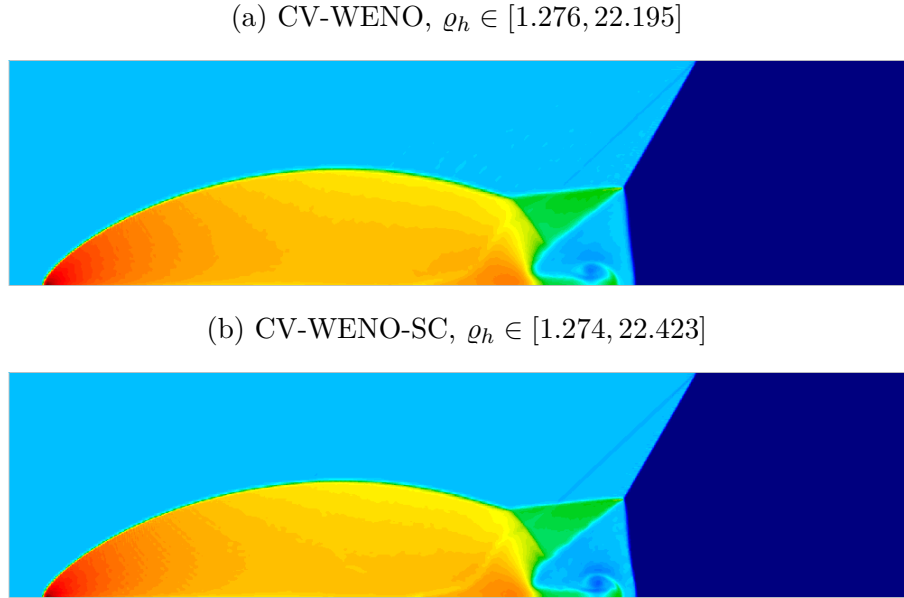


Figure 9: Double Mach reflection, density profiles ρ_h at $t = 0.2$ obtained using discontinuous finite elements with $E_h = 384 \cdot 96$ and $p = 2$.

of cell-level reconstructions are associated with mesh vertices rather than edges or faces, allowing information from vertex neighbors to be incorporated without increasing the number of candidates. The quadrature-weight scaling provides a computationally efficient alternative to subcell-based strategies by locally adjusting dissipation at quadrature nodes. More dissipation is applied near sharp features using a pointwise measure of solution smoothness, similarly to classical WENO schemes. The new features improve the shock-capturing capabilities of the dissipation-based WENO stabilization that we proposed in [45], using its smoothness sensor to control the total amount of dissipation inside each cell. If necessary, preservation of global bounds can be enforced using the convex limiting methodology presented in [42].

Acknowledgments

The work of Dmitri Kuzmin was supported by the German Research Foundation (DFG) within the framework of the priority research program SPP 2410 under grant KU 1530/30-1.

References

- [1] GLVis: Opengl finite element visualization tool. glvis.org.
- [2] N. A. Adams and K. Shariff. A high-resolution hybrid compact-ENO scheme for shock-turbulence interaction problems. *J. Comput. Phys.*, 127(1):27–51, 1996.
- [3] R. Anderson, J. Andrej, A. Barker, J. Bramwell, J.-S. Camier, J. Cerveny, V. Dobrev, Y. Dudouit, A. Fisher, T. Kolev, W. Pazner, M. Stowell, V. Tomov, I. Akkerman, J. Dahm, D. Medina, and S. Zampini. MFEM: A modular finite element methods library. *Computers & Mathematics with Applications*, 81:42–74, 2021.
- [4] J. Andrej, N. Atallah, J.-P. Bäcker, J.-S. Camier, D. Copeland, V. Dobrev, Y. Dudouit, T. Duswald, B. Keith, D. Kim, T. Kolev, B. Lazarov, K. Mittal, W. Pazner, S. Petrides, S. Shiraiwa, M. Stowell, and V. Tomov. High-performance finite elements with MFEM. *The International Journal of High Performance Computing Applications*, 38(5):447–467, 2024.
- [5] S. Badia and J. Bonilla. Monotonicity-preserving finite element schemes based on differentiable nonlinear stabilization. *Comput. Methods Appl. Mech. Eng.*, 313:133–158, 2017.
- [6] S. Badia and A. Hierro. On monotonicity-preserving stabilized finite element approximations of transport problems. *SIAM J. Sci. Comput.*, 36:A2673–A2697, 2014.
- [7] D. S. Balsara, S. Garain, V. Florinski, and W. Boscheri. An efficient class of WENO schemes with adaptive order for unstructured meshes. *J. Comput. Phys.*, 404:109062, 2020.
- [8] D. S. Balsara, S. Garain, and C.-W. Shu. An efficient class of WENO schemes with adaptive order. *J. Comput. Phys.*, 326:780–804, 2016.
- [9] G. R. Barrenechea, V. John, and P. Knobloch. A local projection stabilization finite element method with nonlinear crosswind diffusion for convection-diffusion-reaction equations. *ESAIM Math. Model. Numer. Anal.*, 47:1335–1366, 2013.
- [10] G. R. Barrenechea and F. Valentin. Consistent local projection stabilized finite element methods. *SIAM J. Numer. Anal.*, 48(5):1801–1825, 2010.

- [11] R. Borges, M. Carmona, B. Costa, and W. S. Don. An improved weighted essentially non-oscillatory scheme for hyperbolic conservation laws. *J. Comput. Phys.*, 227(6):3191–3211, 2008.
- [12] M. Braack and E. Burman. Local projection stabilization for the Oseen problem and its interpretation as a variational multiscale method. *SIAM J. Numer. Anal.*, 43:2544–2566, 2006.
- [13] P. Clément. Approximation by finite element functions using local regularization. *Revue française d'automatique, informatique, recherche opérationnelle. Analyse numérique*, 9(R2):77–84, 1975.
- [14] R. Codina. A discontinuity-capturing crosswind-dissipation for the finite element solution of the convection-diffusion equation. *Comput. Methods Appl. Mech. Eng.*, 110:325–342, 1993.
- [15] R. Codina and J. Blasco. A finite element formulation for the Stokes problem allowing equal velocity-pressure interpolation. *Comput. Methods Appl. Mech. Eng.*, 143(3-4):373–391, 1997.
- [16] R. Codina and J. Blasco. Analysis of a stabilized finite element approximation of the transient convection-diffusion-reaction equation using orthogonal subscales. *Comput. Visual Sci.*, 4(3):167–174, 2002.
- [17] O. Friedrich. Weighted essentially non-oscillatory schemes for the interpolation of mean values on unstructured grids. *J. Comput. Phys.*, 144:194–212, 1998.
- [18] L. Fu, X. Y. Hu, and N. A. Adams. A family of high-order targeted ENO schemes for compressible-fluid simulations. *J. Comput. Phys.*, 305:333–359, 2016.
- [19] L. Fu, X. Y. Hu, and N. A. Adams. Targeted ENO schemes with tailored resolution property for hyperbolic conservation laws. *J. Comput. Phys.*, 349:97–121, 2017.
- [20] J. Glaubitz, A. C. Nogueira Jr., J. L. Almeida, R. Cantão, and C. Silva. Smooth and compactly supported viscous sub-cell shock capturing for discontinuous Galerkin methods. *J. Sci. Comput.*, 79(1):249–272, 2019.

- [21] S. Gottlieb, C.-W. Shu, and E. Tadmor. Strong stability-preserving high-order time discretization methods. *SIAM Rev.*, 43:89–112, 2001.
- [22] J.-L. Guermond and B. Popov. Fast estimation from above of the maximum wave speed in the Riemann problem for the Euler equations. *J. Comput. Phys.*, 321:908–926, 2016.
- [23] J.-L. Guermond and B. Popov. Invariant domains and second-order continuous finite element approximation for scalar conservation equations. *SIAM J. Numer. Anal.*, 55:3120–3146, 2017.
- [24] H. Hajduk, D. Kuzmin, T. Kolev, and R. Abgrall. Matrix-free subcell residual distribution for Bernstein finite element discretizations of linear advection equations. *Comput. Methods Appl. Mech. Eng.*, 359:112658, 2020.
- [25] H. Hajduk, D. Kuzmin, T. Kolev, V. Tomov, I. Tomas, and J. N. Shadid. Matrix-free subcell residual distribution for Bernstein finite elements: Monolithic limiting. *Comput. Fluids*, 200:104451, 2020.
- [26] A. Harten and S. Osher. Uniformly high-order accurate nonoscillatory schemes. I. *SIAM J. Numer. Anal.*, 24:279–309, 1987.
- [27] S. Hennemann, A. M. Rueda-Ramírez, F. J. Hindenlang, and G. J. Gassner. A provably entropy stable subcell shock capturing approach for high order split form DG for the compressible Euler equations. *J. Comput. Phys.*, 426:109935, 2021.
- [28] A. K. Henrick, T. D. Aslam, and J. M. Powers. Mapped weighted essentially non-oscillatory schemes: Achieving optimal order near critical points. *J. Comput. Phys.*, 207(2):542–567, 2005.
- [29] D. J. Hill and D. I. Pullin. Hybrid tuned center-difference-WENO method for large eddy simulations in the presence of strong shocks. *J. Comput. Phys.*, 194(2):435–450, 2004.
- [30] X. Hu, Q. Wang, and N. A. Adams. An adaptive central-upwind weighted essentially non-oscillatory scheme. *J. Comput. Phys.*, 229(23):8952–8965, 2010.

- [31] T. J. R. Hughes. Recent progress in the development and understanding of SUPG methods with special reference to the compressible Euler and Navier-Stokes equations. *Int. J. Numer. Meth. Fluids*, 7(11):1261–1275, 1987.
- [32] T. J. R. Hughes and M. Mallet. A new finite element formulation for computational fluid dynamics: IV. A discontinuity-capturing operator for multidimensional advective-diffusive systems. *Comput. Methods Appl. Mech. Eng.*, 58:329–336, 1986.
- [33] A. Jameson, W. Schmidt, and E. Turkel. Numerical solution of the Euler equations by finite volume methods using Runge Kutta time stepping schemes. In *14th Fluid and Plasma Dynamics Conference*. American Institute of Aeronautics and Astronautics, 1981.
- [34] G.-S. Jiang and C.-W. Shu. Efficient implementation of weighted ENO schemes. *J. Comput. Phys.*, 126:202–228, 1996.
- [35] V. John, S. Kaya, and W. Layton. A two-level variational multiscale method for convection-dominated convection-diffusion equations. *Comput. Methods Appl. Mech. Eng.*, 195:4594–4603, 2006.
- [36] C. Johnson, A. Szepessy, and P. Hansbo. On the convergence of shock-capturing streamline diffusion finite element methods for hyperbolic conservation laws. *Math. Comput.*, 54:107–129, 1990.
- [37] P. Knobloch. A generalization of the local projection stabilization for convection-diffusion-reaction equations. *SIAM J. Numer. Anal.*, 48(2):659–680, 2010.
- [38] P. Knobloch and G. Lube. Local projection stabilization for advection-diffusion-reaction problems: One-level vs. two-level approach. *Appl. Numer. Math.*, 59(12):2891–2907, 2009.
- [39] A. Kurganov, G. Petrova, and B. Popov. Adaptive semidiscrete central-upwind schemes for nonconvex hyperbolic conservation laws. *SIAM J. Sci. Comput.*, 29:2381–2401, 2007.
- [40] D. Kuzmin. A vertex-based hierarchical slope limiter for p-adaptive discontinuous Galerkin methods. *J. Comput. Appl. Math.*, 233:3077–3085, 2010.

- [41] D. Kuzmin. Monolithic convex limiting for continuous finite element discretizations of hyperbolic conservation laws. *Comput. Methods Appl. Mech. Eng.*, 361:112804, 2020.
- [42] D. Kuzmin, H. Hajduk, and J. Vedral. A matrix-free convex limiting framework for continuous Galerkin methods with nonlinear stabilization. *arXiv preprint arXiv:2509.04673*, 2025.
- [43] D. Kuzmin and M. Quezada de Luna. Entropy conservation property and entropy stabilization of high-order continuous Galerkin approximations to scalar conservation laws. *Comput. Fluids*, 213:104742, 2020.
- [44] D. Kuzmin and M. Quezada de Luna. Subcell flux limiting for high-order Bernstein finite element discretizations of scalar hyperbolic conservation laws. *J. Comput. Phys.*, 411:109411, 2020.
- [45] D. Kuzmin and J. Vedral. Dissipation-based WENO stabilization of high-order finite element methods for scalar conservation laws. *J. Comput. Phys.*, 487:112153, 2023.
- [46] R. J. LeVeque. High-resolution conservative algorithms for advection in incompressible flow. *SIAM J. Numer. Anal.*, 33:627–665, 1996.
- [47] D. Levy, G. Puppo, and G. Russo. Central WENO schemes for hyperbolic systems of conservation laws. *ESAIM Math. Model. Numer. Anal.*, 33(3):547–571, 1999.
- [48] D. Levy, G. Puppo, and G. Russo. Compact central WENO schemes for multidimensional conservation laws. *SIAM J. Sci. Comput.*, 22(2):656–672, 2000.
- [49] L. Li, H.-B. Wang, G.-Y. Zhao, M.-B. Sun, D.-P. Xiong, and T. Tang. An efficient low-dissipation hybrid central/WENO scheme for compressible flows. *Int. J. Comput. Fluid. Dyn.*, 34(10):705–730, 2020.
- [50] X.-D. Liu, S. Osher, and T. Chan. Weighted essentially non-oscillatory schemes. *J. Comput. Phys.*, 115:200–212, 1994.
- [51] C. Lohmann, D. Kuzmin, J. N. Shadid, and S. Mabuza. Flux-corrected transport algorithms for continuous Galerkin methods based on high order Bernstein finite elements. *J. Comput. Phys.*, 344:151–186, 2017.

- [52] H. Luo, J. D. Baum, and R. Löhner. A Hermite WENO-based limiter for discontinuous Galerkin method on unstructured grids. *J. Comput. Phys.*, 225:686–713, 2007.
- [53] H. Luo, J. D. Baum, and R. Löhner. A discontinuous Galerkin method based on a Taylor basis for the compressible flows on arbitrary grids. *J. Comput. Phys.*, 227:8875–8893, 2008.
- [54] J. Markert, G. Gassner, and S. Walch. A sub-element adaptive shock capturing approach for discontinuous Galerkin methods. *Commun. Appl. Math. Comput.*, 5(2):679–721, 2023.
- [55] MFEM: Modular finite element methods [Software]. mfem.org.
- [56] A. Navas-Montilla, J. Guallart, P. Solán-Fustero, and P. García-Navarro. Exploring the potential of TENO and WENO schemes for simulating under-resolved turbulent flows in the atmosphere using Euler equations. *Comput. Fluids*, 280:106349, 2024.
- [57] M. Nazarov. Convergence of a residual based artificial viscosity finite element method. *Comput. Math. Appl.*, 65:616–626, 2013.
- [58] M. Olshanskii, J.-P. Bäcker, and D. Kuzmin. Gradient-penalty stabilization of sharp and diffuse interface formulations in unfitted Nitsche finite element methods. *Preprint arXiv:2501.16594*, 2025.
- [59] P.-O. Persson and J. Peraire. Sub-cell shock capturing for discontinuous Galerkin methods. In *44th AIAA Aerospace Sciences Meeting and Exhibit*. American Institute of Aeronautics and Astronautics, 2006.
- [60] S. Pirozzoli. Conservative hybrid compact-WENO schemes for shock-turbulence interaction. *J. Comput. Phys.*, 178(1):81–117, 2002.
- [61] J. Qiu and C.-W. Shu. On the construction, comparison, and local characteristic decomposition for high-order central WENO schemes. *J. Comput. Phys.*, 183(1):187–209, 2002.
- [62] J. Qiu and C.-W. Shu. Hermite WENO schemes and their application as limiters for Runge–Kutta discontinuous Galerkin method: One-dimensional case. *J. Comput. Phys.*, 193(1):115–135, 2004.

- [63] J. Qiu and C.-W. Shu. Hermite WENO schemes and their application as limiters for Runge–Kutta discontinuous Galerkin method II: Two dimensional case. *Comput. Fluids*, 34(6):642–663, 2005.
- [64] J. Qiu and C.-W. Shu. Runge–Kutta discontinuous Galerkin method using WENO limiters. *SIAM J. Sci. Comput.*, 26:907–929, 2005.
- [65] A. Quarteroni and A. Valli. *Numerical approximation of partial differential equations*. Springer, 1994.
- [66] A. M. Rueda-Ramírez, W. Pazner, and G. J. Gassner. Subcell limiting strategies for discontinuous Galerkin spectral element methods. *Comput. Fluids*, 247:105627, 2022.
- [67] L. R. Scott and S. Zhang. Finite element interpolation of nonsmooth functions satisfying boundary conditions. *Math. Comput.*, 54(190):483–493, 1990.
- [68] C.-W. Shu and S. Osher. Efficient implementation of essentially non-oscillatory shock-capturing schemes. *J. Comput. Phys.*, 77:439–471, 1988.
- [69] C.-W. Shu and S. Osher. Efficient implementation of essentially non-oscillatory shock-capturing schemes, II. In *Upwind and High-Resolution Schemes*, pages 328–374. Springer, 1989.
- [70] G. A. Sod. A survey of several finite difference methods for systems of nonlinear hyperbolic conservation laws. *J. Comput. Phys.*, 27:1–31, 1978.
- [71] M. Sonntag and C.-D. Munz. Shock capturing for discontinuous Galerkin methods using finite volume subcells. In *Finite Volumes for Complex Applications VII - Elliptic, Parabolic and Hyperbolic Problems*, pages 945–953. Springer, 2014.
- [72] E. F. Toro. *Riemann solvers and numerical methods for fluid dynamics: a practical introduction*. Springer Science & Business Media, 2013.
- [73] P. Tsoutsanis. Stencil selection algorithms for WENO schemes on unstructured meshes. *J. Comput. Phys.: X*, 4:100037, 2019.

- [74] J. Vedral. Dissipative WENO stabilization of high-order discontinuous Galerkin methods for hyperbolic problems. *Preprint arXiv:2309.12019*, 2023.
- [75] J. Vedral, A. Rupp, and D. Kuzmin. Strongly consistent low-dissipation WENO schemes for finite elements. *Appl. Numer. Math.*, 210:64–81, 2025.
- [76] F. Vilar and R. Abgrall. A posteriori local subcell correction of high-order discontinuous Galerkin scheme for conservation laws on two-dimensional unstructured grids. *SIAM J. Sci. Comput.*, 46:A851–A883, 2024.
- [77] Z.-H. Wan, L. Zhou, and D.-J. Sun. Robustness of the hybrid DRP-WENO scheme for shock flow computations. *Int. J. Numer. Meth. Fluids*, 70(8):985–1003, 2012.
- [78] P. Woodward and P. Colella. The numerical simulation of two-dimensional fluid flow with strong shocks. *J. Comput. Phys.*, 54:115–173, 1984.
- [79] X. Zhang and C.-W. Shu. On positivity-preserving high order discontinuous Galerkin schemes for compressible Euler equations on rectangular meshes. *J. Comput. Phys.*, 229:8918–8934, 2010.
- [80] X. Zhang and C.-W. Shu. Maximum-principle-satisfying and positivity-preserving high-order schemes for conservation laws: Survey and new developments. *Proc. R. Soc. A*, 467:2752–2776, 2011.
- [81] X. Zhang, Y. Xia, and C.-W. Shu. Maximum-principle-satisfying and positivity-preserving high order discontinuous Galerkin schemes for conservation laws on triangular meshes. *J. Sci. Comput.*, 50:29–62, 2012.
- [82] X. Zhong and C.-W. Shu. A simple weighted essentially nonoscillatory limiter for Runge–Kutta discontinuous Galerkin methods. *J. Comput. Phys.*, 232:397–415, 2013.
- [83] J. Zhu and J. Qiu. Hermite WENO schemes and their application as limiters for Runge–Kutta discontinuous Galerkin method, III: Unstructured meshes. *J. Sci. Comput.*, 39:293–321, 2009.

- [84] J. Zhu and J. Qiu. A new fifth order finite difference WENO scheme for solving hyperbolic conservation laws. *J. Comput. Phys.*, 318:110–121, 2016.
- [85] J. Zhu and J. Qiu. New finite volume weighted essentially nonoscillatory schemes on triangular meshes. *SIAM J. Sci. Comput.*, 40(2):A903–A928, 2018.
- [86] J. Zhu, J. Qiu, C.-W. Shu, and M. Dumbser. Runge–Kutta discontinuous Galerkin method using WENO limiters II: Unstructured meshes. *J. Comput. Phys.*, 227(9):4330–4353, 2008.
- [87] J. Zhu, X. Zhong, C.-W. Shu, and J. Qiu. Runge–Kutta discontinuous Galerkin method with a simple and compact Hermite WENO limiter on unstructured meshes. *Commun. Comput. Phys.*, 21:623–649, 2017.
- [88] Z. Zou, J. Zhu, and C. Wang. High-order finite-volume multi-resolution WENO schemes on mixed-element unstructured meshes for simulating two-dimensional compressible flows. *Commun. Appl. Math. Comput.*, pages 1–22, 2025.